Identification of magnetic dopants on the surfaces of topological insulators: Experiment and theory for Fe on Bi_{2}Te_{3}(111)

D. West, Y. Y. Sun, S. B. Zhang, T. Zhang, Xucun Ma, P. Cheng, Y. Y. Zhang, X. Chen, J. F. Jia, and Q. K. Xue

Phys. Rev. B **85**, 081305 — Published 14 February 2012
DOI: 10.1103/PhysRevB.85.081305

Identification of Magnetic Dopants on the Surfaces of Topological Insulators: Experiment and Theory for Fe on Bi_2Te_3(111)

D. West, Y.Y. Sun, S. B. Zhang*

Department of Physics, Applied Physics, and Astronomy, Rensselaer Polytechnic Institute, Troy, New York 12180, USA

T. Zhang, Xucun Ma

Institute of Physics, The Chinese Academy of Sciences, Beijing 100190, China

P. Cheng, Y. Y. Zhang, X. Chen, J. F. Jia, and Q. K. Xue

Department of Physics, Tsinghua University, Beijing 100084, China

Abstract

Magnetic impurities are crucial for probing spin-polarized topological surface states. Scanning tunneling microscopy (STM) studies of Fe on the Bi_2Te_3(111) surface are preformed and unveil distinct impurity structures of unknown origin which exhibit temperature-dependent characteristics. Using density functional theory with spin-orbit coupling, we show that Fe prefers highly coordinated subsurface configurations. By comparing simulated STM images we can explain the experimental results of both low-temperature deposition, in which Fe exists in metastable states of which only the transition metal-Bi split interstitial is STM visible, and after room-temperature annealing, in which iron forms substitutional Fe_{Bi}.

Pnictogen chalcogenides are the hallmark of three-dimensional topological insulators (TI),[1,2,3,4,5] with energy gaps in the bulk but metallic states on the surface. The surface states have linear dispersion near the Fermi energy giving rise to a Dirac fermion behavior for the charge carriers. The other well-known Dirac fermion system is graphene[6] with great current interest. However, different from graphene, the Dirac fermions on the TI surfaces are protected by time-reversal symmetry, therefore are robust against disorders and deformations. The topological surface states are also qualitatively different from the half-filled dangling-bond states on ordinary insulator surfaces because the crossing of the topological surface states with the Fermi surface is an intrinsic property of the bulk ensured by its Z_2 topological invariant.[7] The realization of three-dimensional TIs has triggered a series of research that touches the most profound aspects of modern physics, such as non-Maxwell electrodynamics, magnetic monopoles, and Majorana fermions.[8,9,10,11,12,13,14] TIs also hold great promise for robust applications in spintronics and quantum computing. For example, the chiral topological surface states[15] are protected from backscattering and localization in the presence of non-magnetic disorders and impurities[16,17].

Different from the more conventional bulk dilute magnetic semiconductor spintronics, here the spin states all reside on the surfaces. Thus, the practical development of spintronic applications for TIs rely on the ability to introduce surface magnetic defects, monitor, and control them by surface techniques such as the scanning tunneling microscopy (STM). Currently, the understanding of such defects is virtually non-existing and the ability to manipulate them is thus very limited.

In this paper, we report STM measurements of the $Bi_2Te_3(111)$ surface after a cold deposition of Fe and those after room-temperature (RT) annealing. Distinctly different STM images are obtained at the two different temperatures. We then apply first-principles density-functional theory, which includes the spin-orbit interaction (SOI), to determine the atomic structures of the magnetic dopant. The combined studies suggest that transition metal impurities on the $Bi_2Te_3(111)$ surface are most stable as substitutional impurities. At low deposition temperatures, however, STM observes the metastable Fe interstitial and Fe-Bi split interstitial. This reflects the inability of the deposited magnetic dopants to overcome the kinetic barriers at low-temperature to reach their respective low-energy configurations.

Our experiments were carried out in an ultrahigh vacuum low temperature STM system equipped with molecular beam epitaxy (MBE) for thin film sample preparation (Unisoku). The single crystalline thin films of Bi_2Te_3 were grown on Si(111) substrate under Te-rich condition by MBE. Details of the growth conditions are described elsewhere.[18] All the Bi_2Te_3 films discussed in this work have a thickness of 100 nm. The scanning tunneling spectroscopy show that the Fermi level lies within the bulk gap and the Dirac point is located at -0.2 eV below the Fermi level, suggesting that the films are a bulk insulator.[17] Submonolayer Fe was deposited on the clean surface of the film at a substrate temperature of 50 K by direct current heating of a home-made Ta boat. The STM images were acquired in constant current (100 pA) mode at 4 K.

Our calculations are based on density functional theory with the Perdew-Burke-Ernzerhof approximation.[19] Interactions between ion cores and valence electrons are described by the projector augmented wave (PAW) method,[20,21] as implemented in the VASP package.[22,23] Plane-waves with a kinetic energy cutoff of 300 eV were used as the basis set. The SOI was implemented in the all-electron part of the PAW Hamiltonian within the muffin tin spheres. We used a (5x5) surface cell with two quintuple slabs containing 100 Bi and 150 Te atoms and one special k-point at (7/24, 1/12, 0), which yields a total-energy difference less than 0.02 eV per supercell as compared with calculations using a (3x3x1) Monkhorst-Pack k-point grid.[24] The atoms in the topmost four layers are allowed to relax with other atoms fixed at their respective bulk positions. The convergence criterion for the structural relaxations is 0.025 eV/Å.

The impurity formation energy is calculated according to,[25]

$$\Delta E = E(\mathrm{defect}) - E(\mathrm{defect\text{-}free}) + n\mu_{\mathrm{Bi/Te}} - \mu_{\mathrm{Fe}},$$

where E(defect) and E(defect-free) are total energies of the surface with and without the defect, μ's are the atomic chemical potentials, and n equals one for Fe_{Bi} and Fe_{Te} but zero for interstitials (or adatoms). We take μ_{Fe} and μ_{Bi} to be their total energies per atom in the corresponding bulk phases, while μ_{Te} is obtained by the relation $2\mu_{Bi} + 3\mu_{Te} = E(Bi_2Te_3)$, where $E(Bi_2Te_3)$ is the total-energy of bulk Bi_2Te_3 per molecular formula.

Figure 1 shows the STM images for Fe (a) before and (b) after RT annealing. Before annealing, the Fe gives rise to images with a single bright spot (termed Type I), indicated by the white arrows in Fig. 1 (a). From inspection, larger clover-shaped patterns can also be seen; however, it should be noted that these are not Fe related, as they exist in non-deposited samples.

After RT annealing, the Fe related image qualitatively changes from a single bright spot to the dark-centered triangles shown in Fig. 1 (b) (termed Type II), which also become bias sensitive (see below).

Bi_2Te_3 has a layered structure consisting of quintuple slabs;[4] each consists of three layers of Te and two layers of Bi (see Fig. 2). To determine the defects responsible for the observed STM images, we have studied surface adatoms: T_1 = directly above a Te, H_3 = directly above a second layer Te, and T_4 = directly above a first layer Bi, as well as Fe substitution for Bi (Fe_{Bi}) and Te (Fe_{Te}), subsurface interstitial (I), and split interstitial (I_{split}). Fe_{Bi} was found to be the lowest energy defect configuration. Alternatively, Fe_{Te} and the T_1 were found to be quite high in energy, both approximately 2.7 eV higher in energy than Fe_{Bi}. Note that the results here correspond to the Bi-rich growth condition (i.e., μ_{Bi} is that of bulk Bi). Deviation from this condition lowers the formation energy of Fe_{Bi}, increases the formation energy of Fe_{Te}, and leaves the interstitial configurations unchanged. The high energies of Fe_{Te} and the T_1 indicate that Fe prefers high-coordination configurations. This is further indicated by both the H_3 and T_4 geometries (see Fig. 3), instead of staying above the surface, Fe settles at or below the surface, becoming seven- or four-fold coordinated, respectively. Note that this is in contrast to the role that transition metals often play on the surface of semiconductors. From Table I we can see that with the exception of T_1, the interstitial configurations are found to be quite similar in formation energy with H_3, T_4, I, and I_{split}, differing by less than 0.15 eV. Additionally, they were all found to be donors, which is consistent with experimental findings for Fe in Bi_2Te_3.[26]

From Table I, one can also see the effect that the inclusion of SOI has on the calculated formation energies of the studied defects. These results suggest that SOI can have quite a large effect, lowering the formation energies by more than 0.6 eV. However, it should be noted that this effect is not purely due to spin-orbit coupling. Tracking this large energy difference points to an additional contribution due to differences in the band gap. Without SOI, the bulk gap is quite small, 0.3 eV; however, despite the weak interaction between slabs, this gap converges quite slowly with respect to number of slabs, being 0.77 eV with two slabs. This unphysically large gap could potentially lead to a great overestimation of the energy of neutral donors (having either 1, 2, or even 3 electrons in the conduction band could lead to an overestimation as great as 0.4, 0.8, and 1.2 eV, respectively). On the other hand, the inclusion of SOI reduces the gap to 0.3eV, fixing this error, even when only 2 slabs are present. While there is the potential for large errors in the non spin-orbit calculations, in actuality, since the donors are relatively deep comparted to the gap, the overestimation is substantially smaller. By depopulating the defect levels and calculating the formation energies of select charged defects with and without SOI, we can approximate how much of this energy difference is purely due to SOI. In this case, we find that the effect of SOI is smaller and more consistent, for I^{3+}, I_{split}^{2+}, and Fe_{Bi}, the inclusion of SOI reduces the formation energies by .28, .24, and .21 eV, respectively.

To compare with experiment, we simulate the STM images based on the theory of Tersoff and Hamann.[27] Surprisingly, however, a number of the defects investigated produce little or no discernable STM images. Simulated STM images for the low energy intestitials: H_3, T_4, I, and I_{split} (at a bias of −0.4 eV), are shown in Fig. 3. Except for I_{split}, none of the images can be positively identified as having an impurity on a clearly-defined lattice site. These "null" results can be qualitatively understood if we recall that the main character of the states near the valence band edge is that of a Te on the lattice site, not Fe. Thus, (i) the Fe interstitial will naturally not show up, as it is buried underneath surface Te and Bi, while (ii) the H_3, and (iii) T_4, adatom will not show up due to their weak representation in this energy range, despite their relative closeness to the surface. The one dopant that will show up in Fig. 3 is I_{split} but only because here we are actually seeing the Bi which is pushed up by the Fe from underneath. Charge density plot in Fig. 3 further reveals that the image for I_{split} comes from a Bi-Fe hybrid state with Bi orbital *p*-character. If we compare the simulated STM images with experiment shown at the bottom of Fig. 3, we may assign the observed Type-I Fe to I_{split}.

The upper panel of Figure 4 shows the experimental images of Type-II Fe dopant at two different biases: (a) −0.4 V (filled states) and (b) +0.4 V (empty states), respectively. The nature of the images determines that none of the dopant models in Fig. 3 can explain the experimental observation. However, these images do compare favorably with those simulated for Fe_{Bi} at the corresponding biases, as shown in the lower panel of Figs. 4 (a) and (b). At first glance, it might be a bit surprising that a substitutional Fe would yield the pronounced STM images. A closer examination of the dopant charge density reveals that the results here are nonetheless consistent with those in Fig. 3. The key is that Fe_{Bi} is underneath surface Te. What has been experimentally observed at a negative bias is the surface Te states whose energies have been shifted by the underneath Fe. The three-fold symmetry of the experiment also agrees with the model: namely, if not because of the three Te, the predominant feature of the image should be a single spot. At the positive bias, no Te state can appear. In the absence of the Fe states, the image appears as a black triangular hole, which also agrees with experiment.

Combining the results in Figs. 3 and 4, we identify the Type-I Fe as I_{split} and Type-II Fe as Fe_{Bi}. These assignments agree with the calculated energetics: namely, at low deposition temperature, Fe cannot displace Bi to assume the lowest energy configuration. Instead, it remains as adatoms or simply piggybacks on a lattice Bi to form metastable I_{split}. Note that here all Fe adatom configurations exist but only I_{split} is STM detectable. After annealing, Bi will be displaced and the system reaches the global minimum-energy configuration that is Fe_{Bi}. The low energy configuration of Fe_{Bi} was found to have high spin ($5\mu_B$). Despite the high spin, however, the energy difference between the ferromagnetic and antiferromagnetic states was found to be negligible. For a Fe_{Bi} – Fe_{Bi} separation of approximately 11 angstroms (calculated with two Fe_{Bi} per supercell), the 0 μ_B and 10 μ_B spin states differed in energy by less than 1meV. This is consistent with the difficulty in forming a ferromagnetic layer.

In order to get a qualitative picture of the kinetics, we performed nudged elastic band calculations[28,29], albeit out of necessity without SOI, to approximate the barrier for the formation of Fe_{Bi}. In order to form substitutional, Fe must knock-out a Bi, which can then diffuse to some low energy reservoir. The I_{split} configuration is a natural starting point for this process, as from this configuration the Bi can be brought to the surface with the Fe filling in the substitutional location – without the need to form a higher energy Bi subsurface insterstitial or intermediate Bi vacancy. As such, the barrier was calculated from the Fe-Bi split interstitial configuration to Fe_{Bi} with Bi as an adatom at the nearest T_4 site. The energies of the different images along this reaction are shown in Fig. 5, yielding a total barrier of nearly 0.9 eV. The high barrier associated with the removal of Bi, effectively divides the configurations into two temperature domains: in the low-temperature domain the Fe can equilibrate among the various metastable interstitial configurations. In the high-temperature domain this barrier can be overcome, Bi can diffuse away leaving Fe to stay in its globally stable configuration, as Fe_{Bi}.

In summary, combined experimental STM and first-principles study enables the identification, for the first time, the registries and structural properties of a transition metal element on the surface of a topological insulator, Bi_2Te_3(111). We find that the observed STM images are not directly resolving Fe, but rather are the result of host states perturbed by the Fe. We identify both the as-deposited and post anneal configurations which give rise to the observed STM images, as I_{split} and Fe_{Bi}, respectively. The identification of the local atomic structures is of particular importance, as it opens up the prospect of a detailed analysis of spin interactions of the Fe states with the topological surface state, which can be directly compared with experiment.

Acknowledgement: The work at RPI was supported by Department of Energy under grant No. DE-SC0002623 and the CMSN program. The supercomputer time was provided by the CCNI at RPI. The work at IOP and Tsinghua was supported by National Science Foundation and Ministry of Science and Technology of China.

TABLE I. Calculated formation energies (in eV) of Fe related defects on the $Bi_2Te_3(111)$ surface. These values are reported calculated under Bi-rich conditions. Magnetization is also reported in (μ_B), the number reported for SOI is the z-component of the magnetization, other components are less than an order of magnitude smaller than this value.

	No SOI		SOI		$\Delta H^{SOI}-\Delta H^{\text{no SOI}}$
	ΔH(eV)	Mag (μ_B)	ΔH(eV)	Mag (μ_B)	
Fe_{Te}	4.21		4.14		-0.07
T_1	4.19		4.17		-0.02
H_3	1.99	2.1	1.39	3.0	-0.6
T_4	1.96	2.0	1.47	3.4	-0.49
I	2.04	0.0	1.43	0.1	-0.61
$(Bi\text{-}Fe)_{split}$	1.98	4.0	1.53	4.5	-0.45
Fe_{Bi}	1.49	5.0	1.21	4.8	-0.28

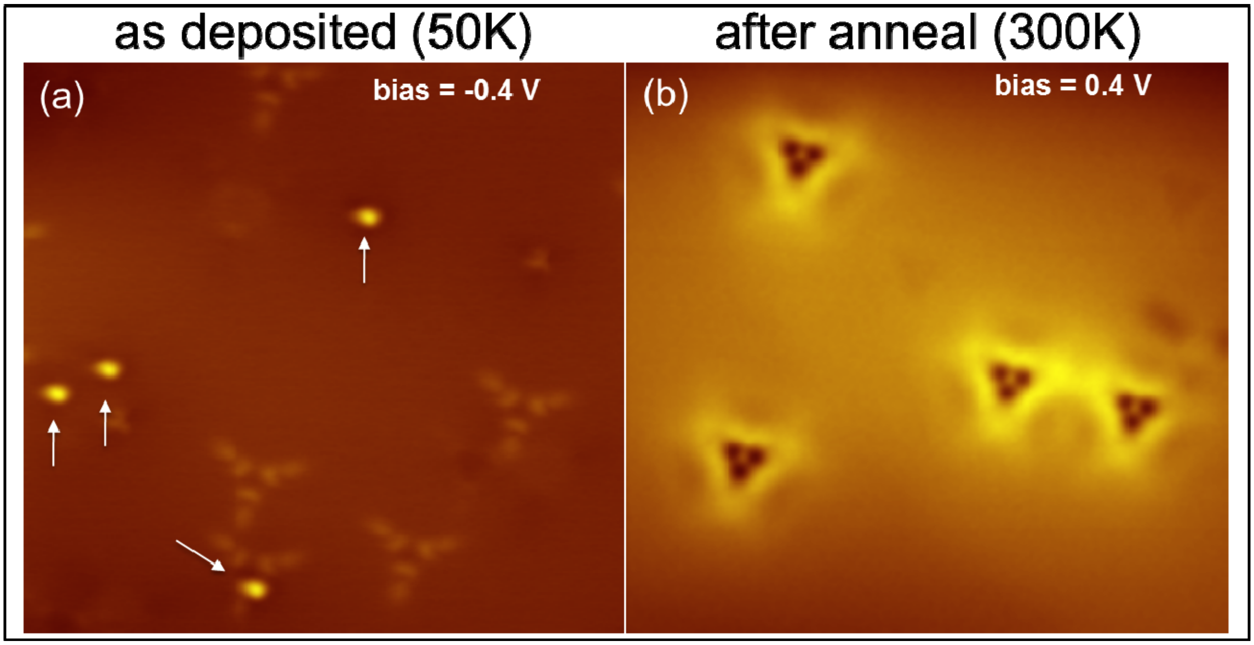

FIG. 1. (color online) STM images (25x25 nm scans) after cold atom Fe deposition on the $Bi_2Te_3(111)$ surface. (a) corresponds to a scan after the initial deposition at 50K and (b) corresponds to a scan after the RT annealing. The scan bias is indicated in each panel.

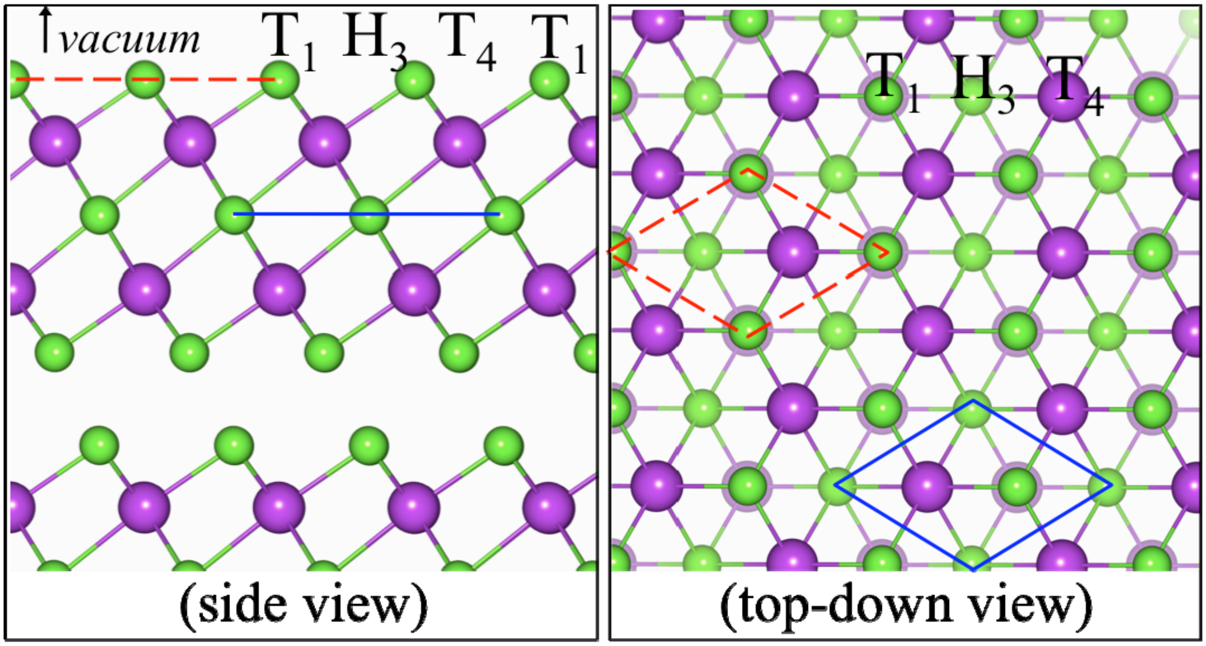

FIG. 2. (color online) Schematic atomic structure of Bi_2Te_3: (left) a side-view and (right) top-view. Te atoms are shown in green (light gray) and Bi atoms are shown in purple (dark gray). The adatom sites T_1, H_3, and T_4 are labeled in both views for reference. The dashed (red) parallelogram indicates the top layer Te, whereas the solid (blue) parallelogram indicates the second layer Te.

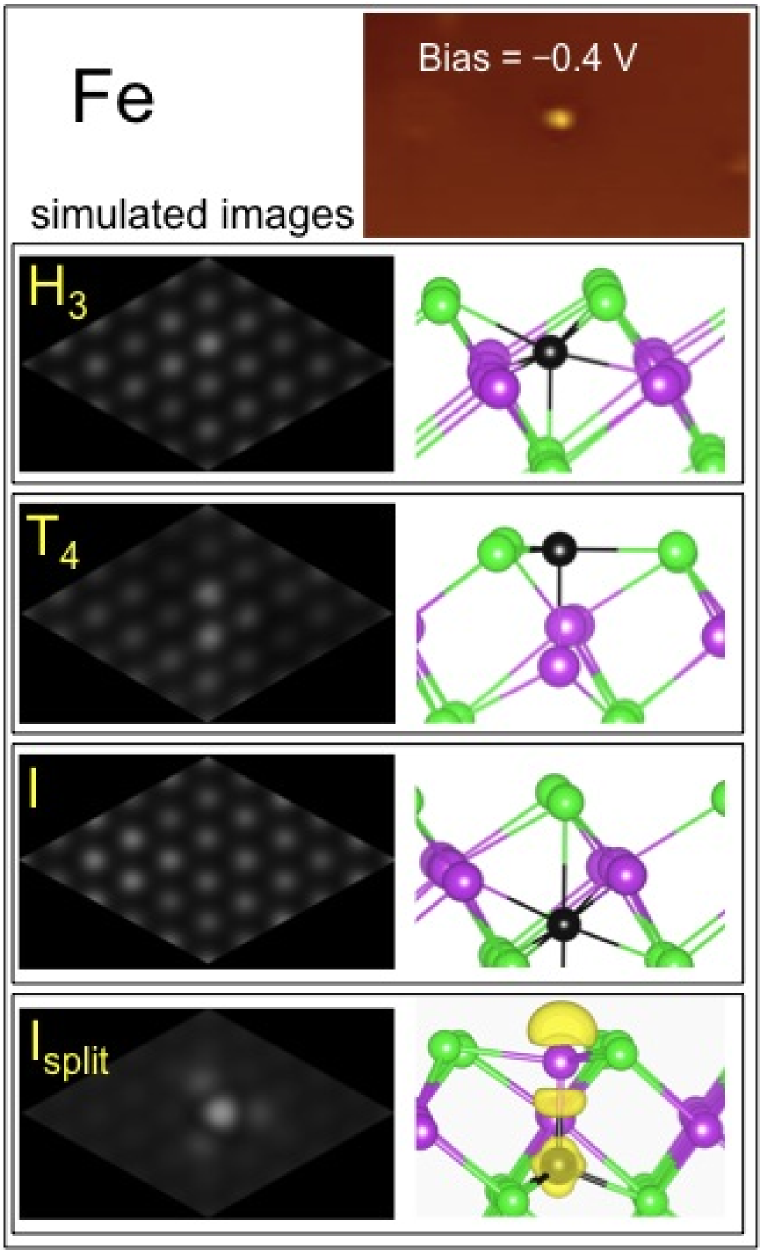

FIG. 3. (color online) top: Experimental low-temperature STM image for Fe at a -0.4V bias (filled states). The simulated STM images, at the same bias, for H_3, T_4, I, and I_{split}, are shown on the left with their corresponding atomic structures on the right (where green = Te, purple = Bi, and black = Fe). No discernable image is obtained except for I_{split} with a single bright spot – comparing favorably to experiment.

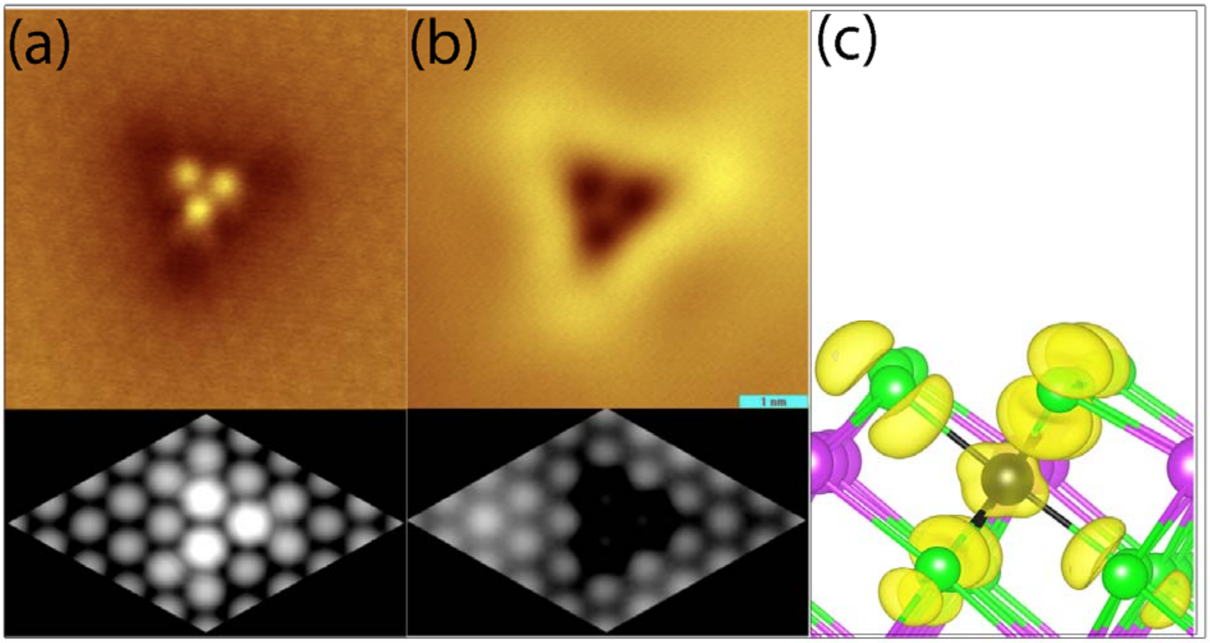

FIG. 4. (color online) (a) and (b) Experimental (above) and simulated (below) STM images at two different biases (–0.4V on left and +0.4V on right) for Type II Fe. The simulated images are obtained from $\mathrm{Fe_{Bi}}$, shown in (c) along with an isosurface of the partial charge density corresponding to the -0.4V bias.

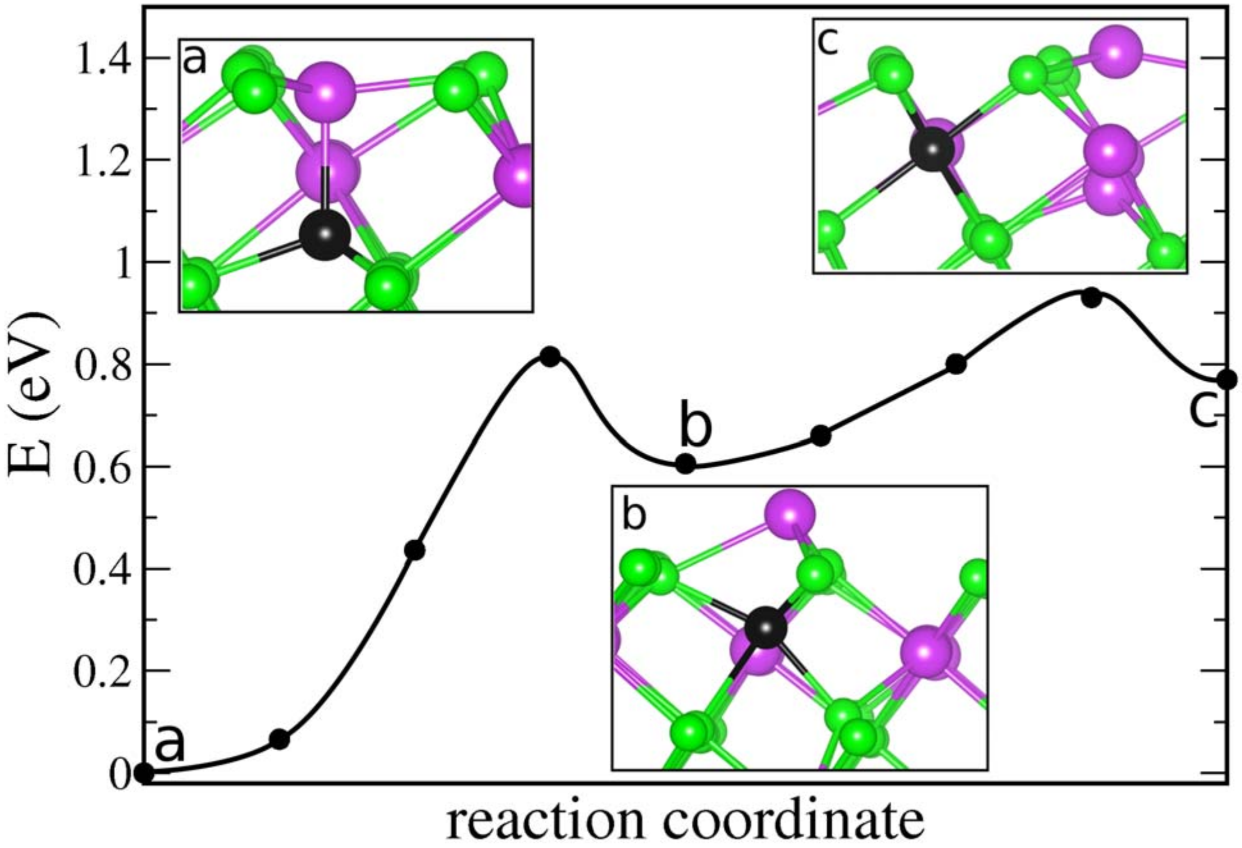

FIG. 5. (color online) NEB calculation of the transition state energy between the I_{split} configuration (depicted as (a)) and Fe_{Bi} with nearby Bi_{adatom} (depicted as (c)). This consists of two calculations, one to and another from the metastable configuration (depicted as (b)). The energies of individual images along the reaction are indicated by points. The curve is added as a guide to the eye.

---

[1] L. Fu and C. L. Kane, Phys. Rev. B **76**, 045302 (2007).

[2] Y. L. Chen, J. G. Analytis, J.-H. Chu, Z. K. Liu, S.-K. Mo, X. L. Qi, H. J. Zhang, D. H. Lu, X. Dai, Z. Fang, S. C. Zhang, I. R. Fisher, Z. Hussain, and Z.-X. Shen, Science **325**, 178 (2009).

[3] H. Zhang, C.-X. Liu, X.-L. Qi, X. Dai, Z. Fang, and S.-C. Zhang, Nature Physics **5**, 438 (2009).

[4] Y. Xia, D. Qian, D. Hsieh, L. Wray, A. Pal, H. Lin, A. Bansil, D. Grauer, Y. S. Hor, R. J. Cava, and M. Z. Hasan, Nature Physics **5**, 398 (2009).

[5] X.-L. Qi, T. L. Hughes, and S.-C. Zhang, Phys. Rev. B **78**, 195424 (2008).

[6] K. S. Novoselov, A. K. Geim, S. V. Morozov, D. Jiang, M. I. Katsnelson, I. V. Grigorieva, S. V. Dubonos, and A. A. Firsov, Nature **438**, 197 (2005).

[7] L. Fu, C. L. Kane, and E. J. Mele, Phys. Rev. Lett. 98, 106803 (2007).

[8] X.-L. Qi and S.-C. Zhang, Phys. Today**,** p33-p38 (Jan. 2010),

[9] M. Z. Hasan and C. L. Kane, **arXiv**:1002.3895 (2010).

[10] J. E. Moore, Nature **464**, 194 (2010).

[11] X.-L. Qi, R. Li, J. Zhang, and S.-C. Zhang, Science **323**, 1184 (2009).

[12] L. Fu and C. L. Kane, Phys. Rev. Lett. **100**, 096407 (2008).

[13] A. R. Akhmerov, J. Nilsson, and C. W. J. Beenakker, Phys. Rev Lett. **102**, 216404 (2009).

[14] L. Fu and C. L. Kane, Phys. Rev. Lett. **102**, 216403 (2009).

[15] D. Hsieh, Y. Xia, L.Wray, D. Qian, A. Pal, J. H. Dil, J. Osterwalder, F. Meier, G. Bihlmayer, C. L. Kane, Y. S. Hor, R. J. Cava, and M. Z. Hasan, Science **323**, 919 (2009).

[16] P. Roushan, J. Seo, C. V. Parker, Y. S. Hor, D. Hsieh, D. Qian, A. Richardella, M. Z. Hasan, R. J. Cava, and A. Yazdani, Nature **460**, 1106 (2009).

[17] T. Zhang, P. Cheng, Xi Chen, J.-F. Jia, X. Ma, Ke He, L. Wang, H. Zhang, Xi Dai, Z. Fang, X. Xie, and Q.-K. Xue, Phys. Rev. Lett. **103**, 266803 (2009).

[18] Y.-Yi Li, G. Wang, X.-G. Zhu, M.-H. Liu, C. Ye, Xi Chen, Ya-Yu Wang, Ke He, Li-Li Wang, X.-C. Ma, H.-J. Zhang, Xi Dai, Z. Fang, X.-C. Xie, Y. Liu, X.-L. Qi, J.-F. Jia, S.-C. Zhang, and Q.-K. Xue, Adv. Mater. (in press).

[19] J. P. Perdew, K. Burke, and M. Ernzerhof, Phys. Rev. Lett. 77, 3865 (1996).

[20] P. E. Blochl, Phys. Rev. B **50**, 17953 (1994).

[21] G. Kresse and D. Joubert, Phys. Rev. B **59**, 1758 (1999).

---

[22] G. Kresse and J. Hafner, Phys. Rev. B **47**, 558 (1993).

[23] G. Kresse and J. Furthmuller, Phys. Rev. B **54**, 11169 (1996).

[24] H. J. Monkhorst and J. D. Pack, Phys. Rev. B **13**, 5188 (1976).

[25] S. B. Zhang and J. E. Northrup, Phys. Rev. Lett. **67**, 2339 (1991).

[26] V. A. Kulbachinskii, A. Yu. Kaminskii, A. Kindo, Y. Narumi, K. Suga, P. Lostak, and P. Svanda, Physica B, **311**, 292 (2002).

[27] J. Tersoff and D. R. Hamann, Phys. Rev. B 31, 805 (1985).

[28] G. Henkelman and H. Jonsson, J. Chem. Phys. **113**, 9978 (2000).

[29] R. A. Olsen, G. J. Kroes, G. Henkelman, A. Arnaldsson, and H. Jonsson, J. Chem. Phys. **121**, 9776 (2004).